Electrical Power and Energy Systems 177 (2026) 111782

Contents lists available at ScienceDirect

International Journal of Electrical Power and Energy Systems

journal homepage: www.elsevier.com/locate/ijepes

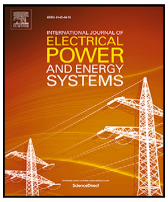

Full-order modeling and design-oriented stability analysis of dual-loop grid-forming Type-3 wind generators

Emanuele Fedele [a],*, Nicola Campagna [b], Giuseppe Bossi [c], Renato Rizzo [a], Rosario Miceli [b], Alfonso Damiano [c]

[a] Dept. of Electrical Engineering and Information Technology, University of Naples Federico II, Via Claudio 21, 80125, Napoli, Italy
[b] Dept. of Engineering, University of Palermo, Viale delle Scienze 7, 90128, Palermo, Italy
[c] Dept. of Electrical and Electronic Engineering, University of Cagliari, Via Marengo 2, 09123, Cagliari, Italy

ARTICLE INFO

Keywords:
Type-3 wind generator
Grid-forming control
Impedance modeling
Stability analysis
Robust control design

ABSTRACT

As the penetration of renewable energy increases, Type 3, wind turbines using doubly fed induction generators are required to support grid stability, with grid-forming control (GFM) emerging as an attractive solution. This paper provides a comprehensive small-signal model and design-oriented stability analysis of a Type-3 wind generator system with dual-loop GFM control. The full-order model offers a flexible representation of the GFM Type-3 system accounting for grid frequency disturbances and full coupling between rotor-side and grid-side converters. It is flexibly adapted to the calculation of generator input admittance and of several closed-loop transfer functions, which are used to assess internal and external stability margins and the influence of grid parameters on the closed-loop system dynamics across a wide frequency range. Extensive time-domain EMT simulations in MATLAB/Simulink are performed to validate the study. The presented analysis provides practical guidelines for the design of a stable Type-3 generator GFM control with specified inertial and damping characteristics under different grid parameters.

1. Introduction

The growing integration of renewables such as wind energy introduces new challenges in maintaining grid stability. With traditional power plants gradually being phased out, the grid loses the inherent stability provided by the inertia of large synchronous generators [1]. Grid-Forming (GFM) control stands as promising solutions for the large-scale integration of renewables [2], as it mimics the inherent features of traditional synchronous generators.

The predominant variable-speed wind turbine systems (WTS) are based on the Type-3 and Type-4 configurations [3]. Type-3 wind turbine systems use Doubly-Fed Induction Generators (DFIGs) for cost-effective onshore setups, while Type-4 uses Permanent-Magnet Synchronous Generators (PMSGs) for offshore applications [4]. Grid-Forming (GFM) control is applied to DFIGs for grid support and weak-grid operation [5], typically through single-loop rotor flux control [6–8]. In single-loop GFM control schemes, the magnitude and phase of the virtual control voltage computed by outer power control loops is directly used as RSC modulation voltage, without inner current-regulation loops. Although simple, single-loop GFM schemes lack current control in case of voltage sags or disturbances. On the other hand, dual-loop GFM schemes offer greater controllability in both normal operation and in the event of grid disturbances [9]. In dual-loop GFM schemes, the virtual voltage is further processed by additional inner control layers, which include a closed-loop current controller, to generate the final modulation voltages. Various dual-loop GFM schemes exist, including PI-based voltage vector, virtual-impedance, and virtual-admittance control. Virtual-admittance control is particularly attractive as it maintains stable performance in strong grids and does not rely on numerical differentiation of the currents [10,11]. However, their application to Type-3 wind generators is still largely unexplored [12].

To maintain stability in WT generators under varying grid conditions, small-signal stability analysis is essential. Key methods include state-space modeling and eigenvalue analysis [13], impedance modeling with the Generalized Nyquist Criterion [14], and transfer-function modeling with frequency-response analysis [15]. State-space modeling offers detailed stability insights but struggles in accounting for digital control delays and becomes complex for larger systems [16,17]. Impedance-based modeling supports complex systems but lacks full closed-loop behavior analysis [18,19]. Closed-loop transfer function modeling effectively assesses grid impacts on control stability and closed-loop dynamics [20]. In Type-3 systems, the DFIG connects the

---

* Corresponding author.
E-mail address: emanuele.fedele@unina.it (E. Fedele).

https://doi.org/10.1016/j.ijepes.2026.111782
Received 20 November 2025; Received in revised form 23 February 2026; Accepted 15 March 2026

stator directly to the grid and the rotor via RSC and GSC [21]. This setup creates coupling between stator and GSC currents, complicating small-signal model accuracy. Simplifications like constant DC voltage [22], or assuming ideal inner current tracking [23] lead to accuracy issues in low and high frequency ranges. Recent full-order models treat GSC and RSC as three-port modules to improve terminal impedance modeling [24,25]. Notably, all the above-mentioned contributions apply to Type-3 wind generators with standard grid-following control, whereas less effort has been devoted to GFM schemes, leaving the analysis of dual-loop GFM control largely unexplored. A small-signal modeling procedure and stability analysis for Type-3 wind generators with virtual synchronous generator control is presented in [6]. However, this work is restricted to a single-loop GFM control structure and only captures low-frequency dynamics on the stator-side, while the grid-side converter behavior is totally discarded. As a consequence, it does not address high-frequency instability mechanisms arising from control delays and weak-grid interactions. A similar single-loop GFM scheme is investigated in [26], but the impact of the DC-link dynamics is neglected, leading to limited accuracy in the medium- and high-frequency ranges. Moreover, no terminal admittance model is derived and the proposed small-signal model is used only for transfer-function-based stability analysis. Although the effect of grid-frequency disturbances on the generator response is examined numerically, it is not embedded in the analytical framework. A slight modification of the single-loop GFM control is proposed in [7], where a current-limiting controller is incorporated into the internal virtual-flux control loop. The stability analysis, however, focuses only on low-frequency dynamics, while high-frequency instability mechanisms revealed by numerical simulations are not adequately captured by the small-signal model, and their mitigation through proper control design is not established. In contrast, [27] considers a dual-loop GFM Type-3 generator and explicitly includes the high-frequency dynamics introduced by the fast inner control loops. Yet, this approach neglects the influence of the slower low-bandwidth outer control loops on both system stability and terminal admittance, and it does not provide closed-loop transfer-function formulations. Furthermore, grid-frequency disturbances are not modeled, and no design-oriented guidelines are offered to ensure adequate stability margins and inertial response of the GFM control, while simultaneously avoiding high-frequency instabilities under different grid-strength conditions.

In conclusion, existing literature on dual-loop GFM Type-3 wind generators either focuses on low-frequency behavior with simplified control representations or captures high-frequency inner-loop dynamics while omitting outer-loop and grid-frequency effects. To fill this gap, this work presents:

- a full-order model of the dual-loop GFM Type-3 wind generator that accounts for the dynamics of the generator, DC link, RSC and GSC control loops, control and PWM delays, and frequency disturbances at the point of common coupling in order to predict unstable dynamics and capture the dominant control couplings over the full control frequency spectrum.
- a design-oriented analysis that reveals the potential instability mechanisms and their connection to control and grid parameters, ranging from the virtual inertia and damping of low-frequency power response of the GFM Type-3 wind generator to middle and high-frequency dynamics introduced by the virtual-admittance and current controllers.

The modeling framework supports both impedance- and transfer-function-based stability analysis over low and high frequencies, and its design-oriented application enables tailoring Type-3 GFM units to achieve required stability margins, inertia, and damping under varying grid conditions.

The remainder of the paper is as follows. The dual-loop GFM Type-3 wind generator system is detailed in Section 2. The full-order small-signal model is established in Section 3. The design-oriented analysis of internal and external stability margins and closed-loop dynamic interactions with the grid is presented in Section 4. A large set of simulation results are presented in Section 5 for validation, and conclusions are drawn in Section 6.

Table 1
System parameters.

Variable	Description	Value
P_n	Rated power	1.5 MW (1 p.u.)
ω_s	Nominal angular frequency	$2\pi 50$ rad/s (1 p.u.)
V_n	Grid voltage	690 Vrms (1 p.u.)
V_{dc}	Nominal DC voltage	1200 V
T_n	Rated torque	11 kN m (1 p.u.)
L_f	Filter inductance	0.5 mH
C_{dc}	DC-link capacitance	20 mF
D_{PSC}	PSC droop gain	$9.8\ 10^4$ kW/Hz (0.05 p.u.)
$[H_{PSC},\ \xi_{PSC}]$	inertia constant and damping	[2 s, 0.7]
k_P^{RPC}	RPC proportional gain	$1.5\ 10^{-5}$ V/VAr
k_I^{RPC}	RPC integral gain	0.0015 V/VAr s
$[L_v,\ R_v]$	VA inductance and resistance	[0.44 mH , 70 mΩ]
ω_c^{CC}	CC bandwidth	200 Hz
ω_c^{DVC}	DVC bandwidth	40 Hz
f_s	Sampling frequency	2000 Hz

2. System description

The configuration of the Type-3 wind generator system is shown in Fig. 1(a). The system includes a wind turbine, the DFIG, power converters, and filters. Stator windings connect directly to the grid, while rotor windings use a back-to-back converter. The control diagrams of the RSC and GSC are shown in Fig. 1(b). The RSC-GFM scheme features the power synchronization control (PSC) and reactive power control (RPC) loops. The PSC loop employs a configurable-natural-droop controller [28]:

$$R_{PSC}(s) = \frac{K_P s + K_I}{s + K_G} \tag{1}$$

to assign inertial time constant H_{PSC}, damping ξ_{PSC}, and droop response D_{PSC}. The angle ϑ_{PSC} defines the control d-q frame position relative to the PCC voltage d-q frame. The RPC loop adjusts the virtual EMF magnitude E using reactive power error. Unlike single-loop GFM control schemes [7,8] where the virtual EMF is directly used for RSC modulation, this work addresses a dual-loop GFM implementation for RSC control. Dual-loop schemes are more complex but allow to shape the generator terminal impedance as required and to maintain tight control of the converter currents in order to prevent overcurrent tripping. In the dual-loop GFM control configuration, the virtual EMF is further processed by internal control loops that consist of a virtual-admittance controller and closed-loop current regulators. In detail, the difference between virtual EMF E and stator voltage $\boldsymbol{v}_s$ is processed by the virtual admittance (VA) block $Y_v = 1/(R_v + sL_v)$ to produce the stator current reference, where L_v and R_v are the virtual inductance and resistance. The stator current references are transformed into rotor current references based on the steady-state d-q DFIG stator equation:

$$\boldsymbol{i}_r^* = \frac{L_s}{L_m}\boldsymbol{i}_s^* + \frac{1}{\omega_s L_m}\begin{bmatrix} 0 & 1 \\ -1 & 0 \end{bmatrix}\boldsymbol{v}_s \tag{2}$$

where L_m and L_s are the mutual and stator inductances, and ω_s is the grid angular frequency. The rotor current control (CC) loop uses standard PI regulators with decoupling and compensation terms and produces the RSC modulating voltage based on the stator-to-rotor dq frame transformation with phase angle $\theta_{PSC} - \theta_r$, with θ_r measured at the generator shaft. The GSC uses a grid-following DC-voltage control (DVC) with PLL for synchronization and a vector current control, which is typical for GFM Type-3 wind systems [12]. The circuit and control parameters of the GFM Type-3 wind generator are given in Table 1.

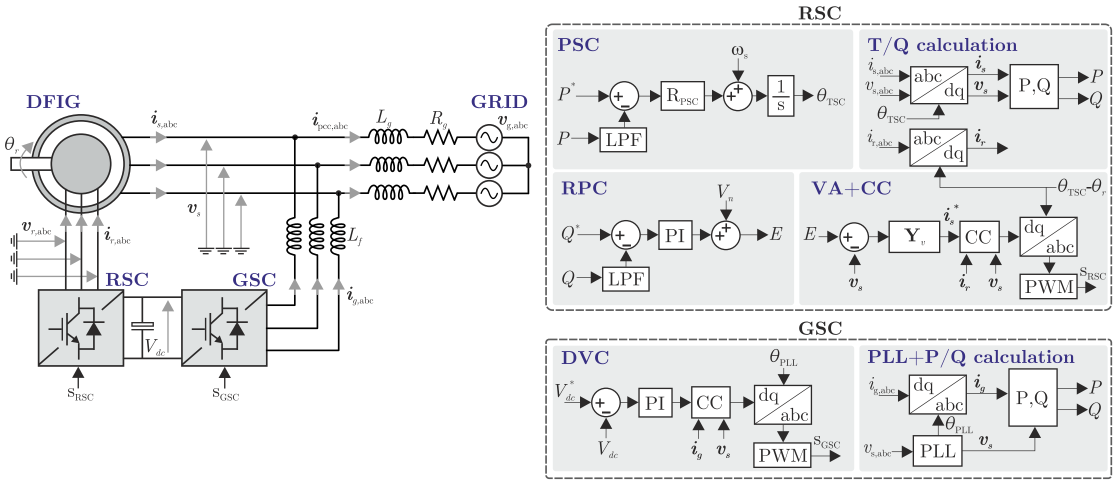

(a) (b)

Fig. 1. Grid-forming Type-3 wind generator: (a) system configuration, (b) RSC and GSC control diagrams.

3. Full-order modeling of dual-loop GFM Type-3 wind generator system

In what follows, variables with a hat $\hat{x}$, are small-signal perturbations around the steady-state value X_0.

3.1. Steady-state linearization point

The steady-state stator voltage magnitude and virtual-EMF phase angle must be obtained based on a given active and reactive power generation level. This is particularly important for a weak-grid connection, where the stator terminal voltage can differ significantly from the rated system voltage. Considering a steady-state operation at given active power $P_{\text{pcc}0}$ and reactive power $Q_{\text{pcc}0}$, the following P/Q power flow equations hold at the PCC:

$$\begin{cases} P_{\text{pcc}0} = \dfrac{3}{2}\dfrac{V_{g0}^2(1-\sigma_{sl})}{\omega_s L_g(1-\sigma_{sl}) + R_g \tan\varphi}\sin\delta_{g0}\cdot \\ \quad\cdot\left(\cos\delta_{g0} + \dfrac{R_g(1-\sigma_{sl}) + \omega_s L_g \tan\varphi}{R_g\tan\varphi + \omega_s L_g(1-\sigma_{sl})}\sin\delta_{g0}\right) \\ Q_{\text{pcc}0} = P_{\text{pcc}0}\tan\varphi \end{cases} \tag{3}$$

where V_{g0} and δ_{g0} are the magnitude of the no-load grid voltage and its phase displacement with the stator voltage, R_g and L_g are the grid resistance and inductance, φ is the power factor angle, and σ_{sl} is the slip. The power flow equations can be solved numerically to obtain the angle δ_{g0}, from which the stator voltages in the natural *d-q* frame are derived as follows:

$$\begin{cases} V_{sd0} = V_{g0}\cos\delta_{g0} + V_{g0}\sin\delta_{g0}\dfrac{R_g(1-\sigma_{sl}) + \omega_s L_g\tan\varphi}{\omega_s L_g(1-\sigma_{sl}) + R_g\tan\varphi} \\ V_{sq0} = 0 \end{cases} \tag{4}$$

Based on the active power flows and stator voltage, the system voltages and currents in the natural *d-q* frame are subsequently derived and define the steady-state linearization point:

$$\boldsymbol{X_0} = \left[I_{sd0}, I_{sq0}, I_{rd0}, I_{rq0}, V_{rd0}, V_{rq0}, I_{gd0}, I_{gq0}, V_{cd0}, V_{cq0}\right]' \tag{5}$$

The detailed expressions of the steady-state voltages and currents as function of the injected power and grid parameters are given in Appendix.

In the GSC control, the displacement between the control and natural *dq* frames is zero in steady state due to the PLL, that is, $\theta_0^{\text{gsc}} = 0$. In the RSC control, a steady-state displacement exists which coincides with the virtual EMF phase angle:

$$\boldsymbol{E_0} = V_{sd0} + \left(R_v + \mathrm{j}\omega_s L_v\right)\left(I_{sd0} + \mathrm{j}I_{sq0}\right) \Rightarrow \theta_0^{\text{rsc}} = \angle\boldsymbol{E_0} \tag{6}$$

The steady-state linearization point and control displacement angle θ are also employed in the forward and inverse linearized frame transformations between control and natural *d-q* frames:

$$\hat{\boldsymbol{x}}^c = \boldsymbol{T_\theta}\hat{\boldsymbol{x}} + \underbrace{\begin{bmatrix} \cos\theta_0 X_{q0} - \sin\theta_0 X_{d0} \\ -\cos\theta_0 X_{d0} - \sin\theta_0 X_{q0} \end{bmatrix}}_{\boldsymbol{k_{x\theta}^c}}\hat{\theta} \tag{7}$$

$$\hat{\boldsymbol{x}} = \boldsymbol{T_\theta^{-1}}\hat{\boldsymbol{x}}^c + \underbrace{\begin{bmatrix} -X_{q0} \\ X_{d0} \end{bmatrix}}_{\boldsymbol{k_{x\theta}}}\hat{\theta} \tag{8}$$

where superscript $\boldsymbol{c}$ denotes the control *d-q* frame, and $\boldsymbol{T_\theta}$ is the steady-state Park transformation matrix:

$$\boldsymbol{T_\theta} = \begin{bmatrix} \cos\theta_0 & \sin\theta_0 \\ -\sin\theta_0 & \cos\theta_0 \end{bmatrix} \tag{9}$$

which concides with the identity matrix for the GSC but not for the RSC.

3.2. Stator channel: RSC and DFIG dynamics

The PSC loop dynamics are given by the power synchronization controller, which computes the instantaneous control-frame phase angle $\hat{\theta}_{PSC}$ based on the error between reference and estimated power:

$$\hat{\theta}_{PSC} = \underbrace{\frac{\left(2K_P + T_s K_I\right) + (T_s K_I - 2K_P)z^{-1}}{\left(T_s K_G + 2\right) + (T_s K_G - 2)z^{-1}}}_{R_{PSC}(z)}\left(\hat{P}^* - \hat{P}_{LPF}\right) \tag{10}$$

where $R_{PSC}(z)$ is the discrete-time implementation of the PSC controller structure in (1), and $\hat{P}_{LPF}$ is the low-pass filtered active power estimation obtained from the measured stator voltages and currents:

$$\hat{P}_{LPF} = \underbrace{\frac{T_s\omega_{LPF}}{1 + T_s\omega_{LPF}\,z^{-1}}}_{G_{LPF}(z)}\left(\boldsymbol{k_{PIs}}\hat{\boldsymbol{i}}_{\boldsymbol{s}} + \boldsymbol{k_{PVs}}\hat{\boldsymbol{v}}_{\boldsymbol{s}}\right) \tag{11}$$

The PSC dynamics and possible variations in the angular grid frequency $\hat{\omega}_g$ at the PCC determine the actual phase displacement $\hat{\theta}_{rsc}$ between RSC control and natural *d-q* frames:

$$\hat{\theta}_{rsc} = \hat{\theta}_{PSC} - \frac{1}{s}\hat{\omega}_g \tag{12}$$

The RPC loop dynamics are given by the reactive power controller:

$$\hat{e} = \underbrace{\left(k_p + k_i T_s \frac{z^{-1}}{1 - z^{-1}}\right)}_{R_Q(z)} \left(\hat{Q}^* - \hat{Q}_{LPF}\right) \tag{13}$$

where $\hat{Q}_{LPF}$ is the low-pass filtered reactive power estimation:

$$\hat{Q}_{LPF} = G_{LPF}(z)\left(\boldsymbol{k_{QIs}}\hat{\boldsymbol{i}}_s + \boldsymbol{k_{QVs}}\hat{\boldsymbol{v}}_s\right) \tag{14}$$

The expressions of the active and reactive power gains $\boldsymbol{k_{PIs}}$, $\boldsymbol{k_{PVs}}$, $\boldsymbol{k_{QIs}}$, and $\boldsymbol{k_{QVs}}$ are given in Appendix. It is important to remark that active and reactive power estimations do not depend on the specific reference frame used for stator currents and voltages. Hence, they are here directly expressed in the natural *d*-*q* frame. The DFIG rotor current reference is the combination of the virtual admittance and stator voltage feed-through terms:

$$\hat{\boldsymbol{i}}_r^* = \frac{L_s}{L_m}\boldsymbol{Y}_v(z)\left(\begin{bmatrix} \hat{e} \\ 0 \end{bmatrix} - \hat{\boldsymbol{v}}_s^c\right) + \underbrace{\frac{1}{\omega_s L_m}\begin{bmatrix} 0 & 1 \\ -1 & 0 \end{bmatrix}}_{\boldsymbol{K_{Vscmp}}} \tag{15}$$

where the detailed equations of the discrete-time virtual admittance matrix are given in Appendix. Ultimately, the dynamics of the inner-loop rotor current control with decoupling and compensation terms is modeled in the control *d*-*q* frame as:

$$\hat{\boldsymbol{v}}_r^c = \underbrace{\left(k_p + k_i T_s \frac{z^{-1}}{1 - z^{-1}}\right)}_{\boldsymbol{G_{cc}^{rsc}}(z)} \mathbf{I}\,(\hat{\boldsymbol{i}}_r^* - \hat{\boldsymbol{i}}_r^c) +$$

$$+ \underbrace{\omega_{sl} L_r' \begin{bmatrix} 0 & -1 \\ 1 & 0 \end{bmatrix}}_{\boldsymbol{K_{dcpl}^{rsc}}} \hat{\boldsymbol{i}}_r^c + \underbrace{\sigma_{sl}\frac{L_m}{L_s}}_{\boldsymbol{K_{Vrcmp}}}\mathbf{I}\,\hat{\boldsymbol{v}}_s^c \tag{16}$$

where L_r' is the transient rotor inductance, $\omega_{sl} = \sigma_{sl}\omega_s$ is the slip angular frequency, $G_{cc}^{rsc}(z)$ is the discrete-time implementation of the PI current controller. The dynamic effects of sampling, computation delay, and RSC power converter are modeled in the natural *d*-*q* frame by the aggregated transfer function $G_d(s) = \mathrm{e}^{-3/2T_s}$. By neglecting the stator resistance, the rotor current dynamics write as (see [21] for details):

$$\hat{\boldsymbol{i}}_r = \underbrace{\begin{bmatrix} R_r + sL_r' & -\omega_{sl}L_r' \\ \omega_{sl}L_r' & R_r + sL_r' \end{bmatrix}^{-1}}_{\boldsymbol{G_{Lr}}(s)}$$

$$\times \left(\hat{\boldsymbol{v}}_r - \underbrace{\begin{bmatrix} -sL_m & \omega_{sl}L_m \\ -\omega_{sl}L_m & -sL_m \end{bmatrix}}_{\boldsymbol{G_{Lm}}(s)} \underbrace{\begin{bmatrix} -sL_s & \omega_s L_s \\ -\omega_s L_s & -sL_s \end{bmatrix}^{-1}}_{\boldsymbol{G_{Ls}}(s)} \hat{\boldsymbol{v}}_s\right) \tag{17}$$

The perturbation in rotor-side active power $\hat{P}_r$ is obtained from the RSC active power linearization:

$$\hat{P}_r = \frac{3}{2}\left(\begin{bmatrix} I_{rd0} \\ I_{rq0} \end{bmatrix}' \hat{\boldsymbol{v}}_r + \begin{bmatrix} V_{rd0} \\ V_{rq0} \end{bmatrix}' \hat{\boldsymbol{i}}_r\right) \tag{18}$$

Substituting (17) into (18) and after some manipulations, the rotor-side power perturbation is expressed as a function of the stator-side voltages and currents:

$$\hat{P}_r = \boldsymbol{k_{PrIs}}(s)\hat{\boldsymbol{i}}_s + \boldsymbol{k_{PrVs}}(s)\hat{\boldsymbol{v}}_s \tag{19}$$

where the detailed expressions of $\boldsymbol{k_{PrIs}}$ and $\boldsymbol{k_{PrVs}}$ are given in Appendix.

3.3. GSC channel: DC and filter dynamics

The small-signal dynamics of the DC link are obtained from the RSC and GSC power balance equation at the DC capacitor node:

$$\hat{v}_{dc} = \underbrace{\frac{1}{sC_{dc}V_{dc0}}}_{G_{dc}(s)} \left(\hat{P}_{gsc} - \hat{P}_r\right) \tag{20}$$

where C_{dc} and V_{dc0} are the DC capacitance and steady-state voltage, and the perturbation of GSC active power is given by:

$$\hat{P}_{gsc} = \underbrace{\frac{3}{2}\begin{bmatrix} I_{gd0} \\ I_{gq0} \end{bmatrix}'}_{\boldsymbol{k_{PcVs}}} \hat{\boldsymbol{v}}_s + \underbrace{\frac{3}{2}\begin{bmatrix} V_{sd0} \\ V_{sq0} \end{bmatrix}'}_{\boldsymbol{k_{PcIg}}} \hat{\boldsymbol{i}}_g \tag{21}$$

The model of the grid-side filter is:

$$\hat{\boldsymbol{i}}_g = \underbrace{\frac{\begin{bmatrix} sL_f + R_f & \omega_s L_f \\ -\omega_s L_f & sL_f + R_f \end{bmatrix}}{(L_f^2 s^2 + L_f^2 w_s^2 + 2L_f R_f s + R_f^2)}}_{\boldsymbol{G_{Lf}}(s)} \left(\hat{\boldsymbol{v}}_s - \hat{\boldsymbol{v}}_c\right) \tag{22}$$

where L_f and R_f are GSC filter inductance and parasitic resistance, respectively. The closed-loop discrete-time PLL dynamics are given by $\hat{\theta}_{PLL} = G_{PLL}(z)\hat{v}_{sq}$, where $G_{PLL}(z)$ is given in Appendix. It defines the actual phase displacement between GSC control and natural *d*-*q* frames as $\hat{\theta}_{gsc} = \hat{\theta}_{PLL} - \hat{\omega}_g/s$. The dynamics of the DVC and CC loops in the GSC are given by:

$$\hat{\boldsymbol{i}}_g^* = \underbrace{\left(k_p + k_i T_s \frac{z^{-1}}{1 - z^{-1}}\right)\begin{bmatrix} 1 & 0 \end{bmatrix}'}_{\boldsymbol{R_V}(z)} \left(\hat{v}_{dc}^* - \hat{v}_{dc}\right) \tag{23}$$

$$\hat{\boldsymbol{v}}_c^c = \boldsymbol{G_{cc}^{gsc}}(z)(\hat{\boldsymbol{i}}_g^* - \hat{\boldsymbol{i}}_g^c) + \underbrace{\omega_s L_f \begin{bmatrix} 0 & 1 \\ -1 & 0 \end{bmatrix}}_{\boldsymbol{K_{dcpl}^{gsc}}} \hat{\boldsymbol{i}}_c^c + \mathbf{I}\,\hat{\boldsymbol{v}}_s^c \tag{24}$$

Ultimately, small-signal voltage perturbations accounting for the grid impedance at the PCC are expressed by:

$$\hat{\boldsymbol{v}}_s = \underbrace{\begin{bmatrix} sL_g + R_g & \omega_s L_g \\ -\omega_s L_g & sL_g + R_g \end{bmatrix}}_{\boldsymbol{Z_g}(s)} \hat{\boldsymbol{i}}_{\mathbf{pcc}} \tag{25}$$

The dynamics of the complete GFM Type-3 system are represented by the block diagram of Fig. 2. where $\hat{P}^*$, $\hat{Q}^*$, and $\hat{v}_{dc}^*$ are control references, $\hat{\omega}_g$ is the grid frequency disturbance, and $\hat{\boldsymbol{v}}_s$ can be either set as an external voltage disturbance or obtained from the grid impedance model, as detailed in later sections. The DFIG channel includes the linearized small-signal block models of the PSC, RPC, and inner VA and CC loops. The RSC control determines the rotor-side voltage $\hat{\boldsymbol{v}}_r$ which, together with the external stator voltage $\hat{\boldsymbol{v}}_s$ is input to the DFIG model, which outputs the stator and rotor currents $\hat{\boldsymbol{i}}_s$ and $\hat{\boldsymbol{i}}_r$. On the GSC channel, the cascaded DCV and current loops set the GSC voltage $\hat{\boldsymbol{v}}_c$ which, together with the stator voltage, determine the GSC current $\hat{\boldsymbol{i}}_g$ and power $\hat{P}_{gsc}$. The stator and GSC currents are added together to obtain the PCC current. The stator-to-GSC coupling gains are highlighted in yellow and represent the physical channels through which a rotor power perturbation $\hat{P}_r$ is transmitted from the stator to the rotor side and, together with $\hat{P}_{gsc}$, results in DC voltage variation $\hat{v}_{dc}$.

3.4. Aggregated modeling of inner loops

The extended small-signal model and block diagram are simplified by deriving aggregated transfer functions for the inner loops. On the

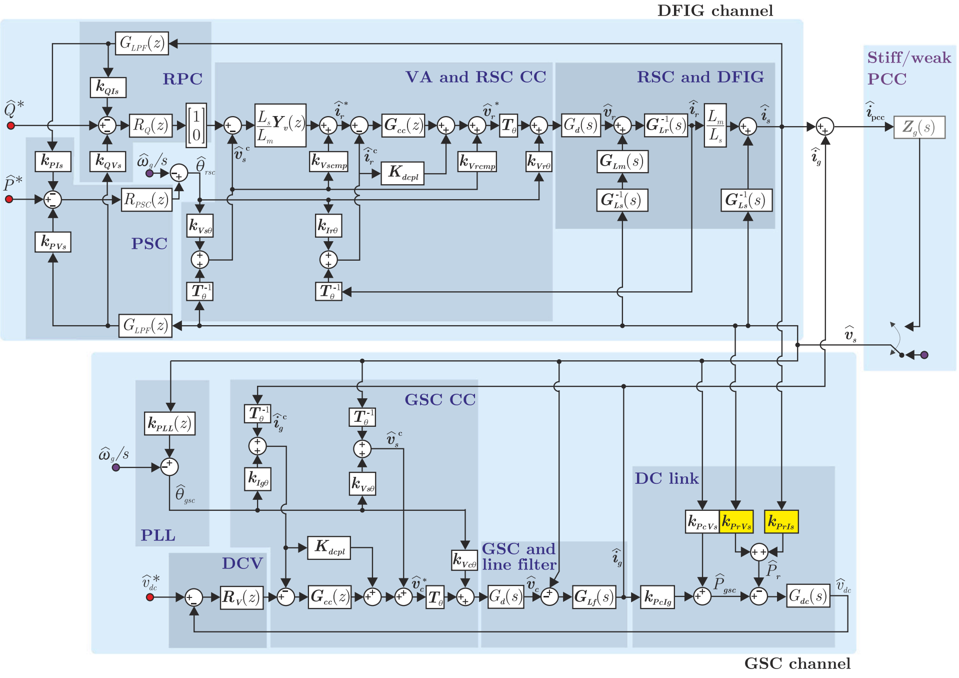

Fig. 2. Block diagram of the dual-loop GFM Type-3 wind generator full-order model.

stator side, the open-loop current-to-PSC angle, current-to-virtual EMF magnitude, and current-to-voltage transfer functions are obtained:

$$\hat{\boldsymbol{i}}_s = \boldsymbol{G}_{is\theta}(s)\hat{\theta}_{rsc} + \boldsymbol{G}_{isE}(s)\hat{E} + \boldsymbol{G}_{isvs}(s)\hat{\boldsymbol{v}}_s \tag{26}$$

where their detailed expressions are reported in the Appendix. These transfer functions do not include the low-frequency behavior which is dictated by the external loops. For example, $\boldsymbol{G}_{isvs}(s)$ coincides with what is reported in [27] to be the stator-side self-admittance. However, the actual stator-side self-admittance should also include the low-bandwidth outer loops, as derived later. Similar transfer functions are derived for the GSC current control loops:

$$\hat{\boldsymbol{i}}_g = \boldsymbol{G}_{igc}(s)\hat{\boldsymbol{i}}_g^* + \boldsymbol{G}_{ig\theta}(s)\hat{\theta}_{gsc} + \boldsymbol{G}_{igvs}(s)\hat{\boldsymbol{v}}_s \tag{27}$$

where detailed expressions of the transfer functions are reported in the Appendix. For instance, $\boldsymbol{G}_{igc}(s)$ represents the dynamics of the grid-side closed-loop current control under stiff PCC voltage. From the compact representation of inner loops, the full-order aggregated model shown in Fig. 3 is obtained, highlighting PSC, RPC, and DCV loop dynamics and mutual interactions. Any changes in control structure affect only specific blocks of outer loops, yielding a flexible modular model that enables straightforward use in the design-oriented stability assessments. It is worth remarking that the aggregated model preserves all the dynamics of the original small-signal model and introduces no approximations, either in the Type-3 generator model or in the grid representation.The full-order aggregated model is utilized in the subsequent section to derive the closed-loop transfer functions and terminal admittance of the GFM Type-3 wind generator under various control parameters and grid conditions.

4. Design-oriented analysis of closed-loop dynamics

This section presents the sensitivity of stability margins and closed-loop dynamics to control and grid parameters, offering insight and practical design guidelines.

4.1. Internal stability

For *internal stability* evaluation of the GFM Type-3 wind generator system, a stiff grid connection (i.e., $\hat{\boldsymbol{v}}_s = 0$) must be considered at the

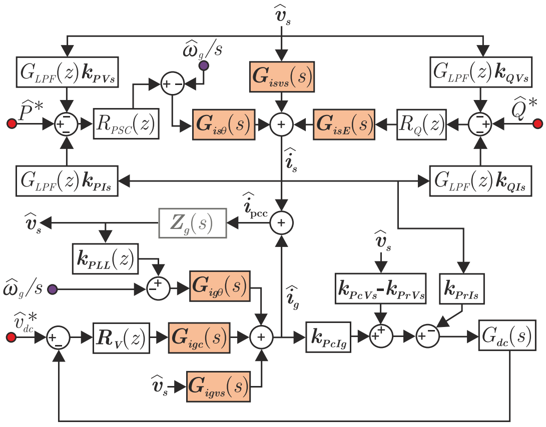

Fig. 3. Aggregated small-signal model.

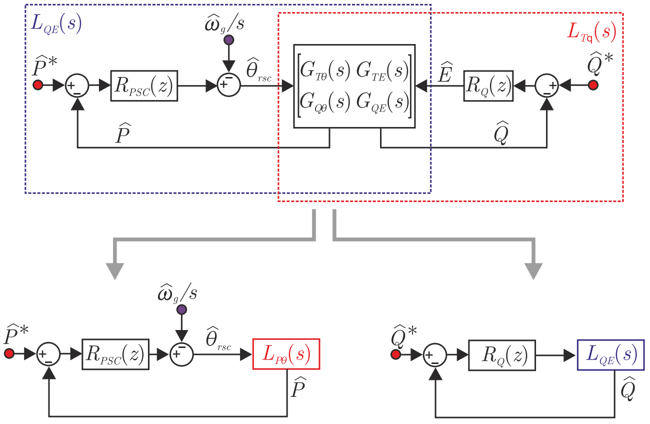

Fig. 4. SISO models for the PSC and RPC control loops.

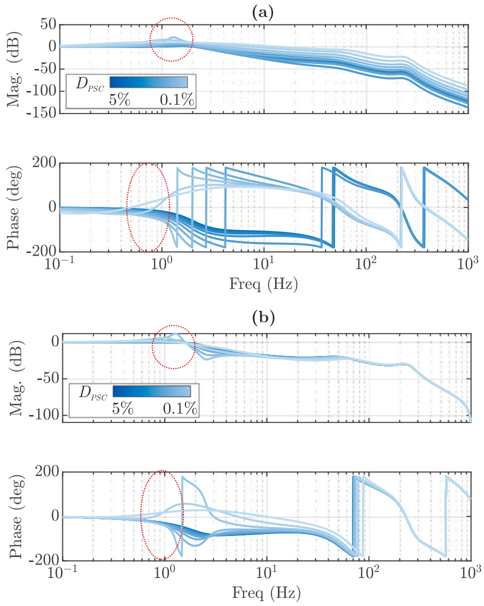

Fig. 5. Closed-loop transfer functions under ideal grid with variable D_{PSC}: (a) PSC loop, (b) RPC loop.

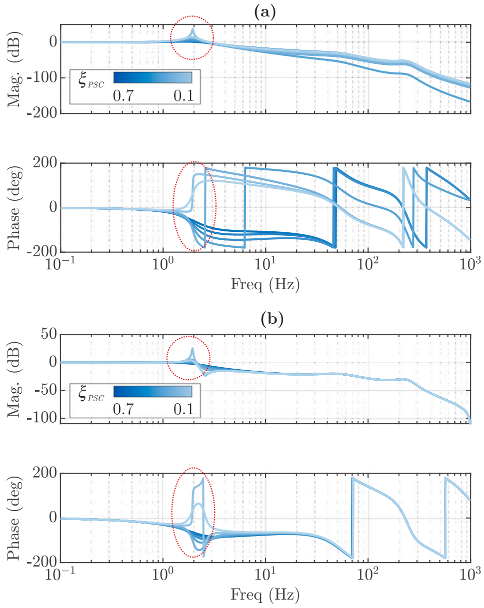

Fig. 6. Closed-loop transfer functions under ideal grid with variable ξ_{PSC}: (a) PSC loop, (b) RPC loop.

PCC. Letting $\hat{\boldsymbol{v}}_s = 0$ in (26) and using the active and reactive power gains yields:

$$\hat{P} = \underbrace{\left(\boldsymbol{k_{PI_s} G_{is\theta}}\right)}_{G_{P\theta}(s)} \hat{\theta}_{rsc} + \underbrace{\left(\boldsymbol{k_{PI_s} G_{isE}}\right)}_{G_{PE}(s)} \hat{E} \tag{28}$$

$$\hat{Q} = \underbrace{\left(\boldsymbol{k_{QI_s} G_{is\theta}}\right)}_{G_{Q\theta}(s)} \hat{\theta}_{rsc} + \underbrace{\left(\boldsymbol{k_{QI_s} G_{isE}}\right)}_{G_{QE}(s)} \hat{E} \tag{29}$$

The above relations reveal a clear coupling between active and reactive power, which is expected from a GFM control scheme. Taking into account only one reference input at a time in the RSC control scheme, single-loop SISO models of the PSC and RPC are derived as shown in Fig. 4, where

$$L_{P\theta} = G_{P\theta} - G_{PE}\frac{G_{LPF}R_Q G_{Q\theta}}{1 + R_Q G_{LPF} G_{QE}} \tag{30}$$

$$L_{QE} = G_{QE} - G_{Q\theta}\frac{G_{LPF}R_{PSC} G_{TE}}{1 + R_{PSC} G_{LPF} G_{T\theta}} \tag{31}$$

Furthermore, an explicit representation of the grid frequency-to-active power transfer function is also derived from the SISO PSC model:

$$\frac{\hat{P}}{\hat{\omega}_g} = -\frac{1}{s}\frac{L_{P\theta}}{1 + R_{PSC}L_{P\theta}} \tag{32}$$

Dynamic equations of active power-to-angle and reactive power-to-EMF are essential for PSC and RPC loop design. Initially, PSC loop design often uses a static model [28], but dynamic modeling is necessary for fine-tuning and to avoid control instability.

Fig. 5 illustrates the internal stability of the PSC and RPC control loops as the PSC droop D_{PSC} decreases from 2.5% to 0.1%. The droop gain significantly impacts the damping of low-frequency poles near 1 Hz, marked by red circles. When D_{PSC} reaches 0.25%, the poles become unstable, indicating potential low-frequency oscillations (LFO). This instability affects both PSC and RPC loops, highlighting their inherent coupling, characteristic of GFM control.

The effect of the PSC damping factor ξ_{PSC} on the PSC and RPC loops is shown in Fig. 6. Lowering the PSC damping factor ($\xi_{PSC} < 0.3$) causes instability in the PSC and RPC loops, leading to a 2–3 Hz LFO mode. Thus, reducing the PSC controller's droop and damping affects LFO stability negatively. Such low-frequency instability mechanisms introduced by outer P/Q controllers are completely neglected in [27], which considers only the high-frequency system dynamics.

Fig. 7 shows the impact of the RPC proportional gain on the closed-loop system dynamics. A transition of k_p^{RPC} from 0.3 to 0.4 p.u. determines negatively damped poles at around 50 Hz and a corresponding unstable synchronous oscillation (SO) mode. This coupling between RPC and SO instability is not reported in [6,7], which addressed only the low-frequency torque dynamics of the GFM Type-3 generator. In the low frequency range, the RPC controller settings have little effect on the closed-loop frequency response.

Fig. 8 shows how the CC bandwidth affects internal stability. A high-frequency oscillation (HFO) mode around 270 Hz becomes unstable when the CC bandwidth increases beyond 300 Hz. Since the current control layer is designed to achieve the highest bandwidth among all layers of the overall GFM control scheme, a correlation with HFO modes is reasonably expected. Being and internal instability mechanism, this HFO arises from the destabilizing effect of computational and PWM delays, which are properly captured by the derived model. A similar analysis is performed considering a sweep in the virtual impedance magnitude and resistance-to-reactance ratio R_v/X_v. The results (not shown) demonstrate that changes in virtual admittance (0.5 to 0.1 p.u.) and R_v/X_v ratio (0.1 to 2 p.u.) do not trigger internal instability in the GFM Type-3 wind generator.

Fig. 9 illustrates that increasing R_v/X_v enhances P/Q coupling at low frequencies, while reducing R_v aids in decoupling active and reactive power. However, a too low R_v can introduce a poorly damped SO mode. The physical mechanism behind this SO oscillation lays in the dynamics introduced by the VA controller. As the R_v/X_v ratio increases, the resistive part of the virtual impedance becomes more significant and provides larger damping to the poles introduced by the VA control block, reducing the settling time after which the VA dynamics reach the steady state. Therefore, a trade-off between SO mode damping and P/Q power decoupling arises when selecting R_v/X_v. Notably, such strong couplings between the VA and CC controllers and the unstable SO and HFO modes are not reported in [6,7], where only the low-frequency inertial response of the GFM wind generator is analyzed for a simple single-loop configuration.

In conclusion, the small-signal model analysis of the GFM Type-3 wind generator reveals its internal stability and control loop interactions. The PSC affects LFO modes, RPC and VA controllers influence the

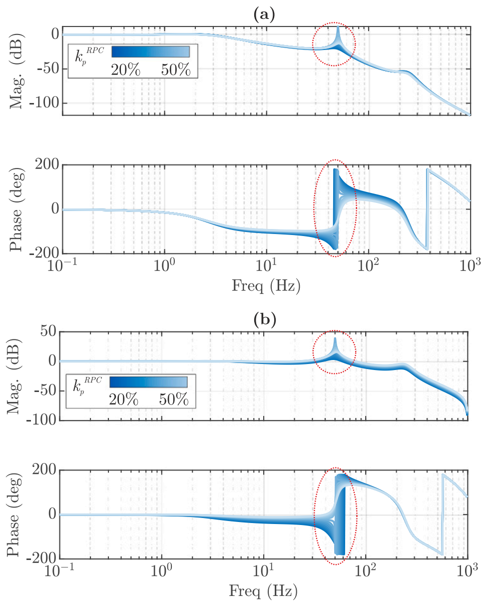

Fig. 7. Closed-loop transfer functions under ideal grid with variable k_P^{RPC}: (a) PSC loop, (b) RPC loop.

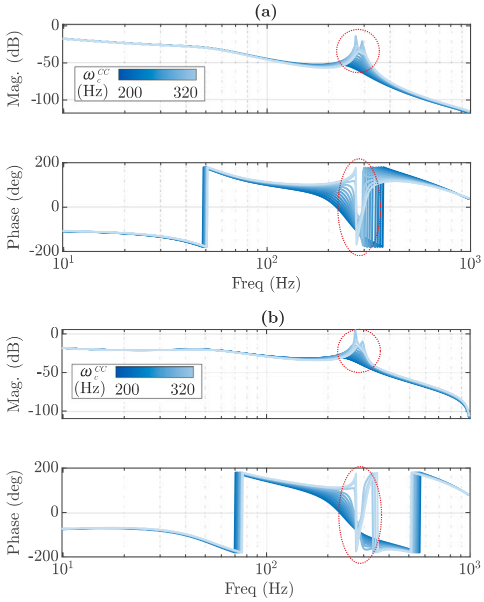

Fig. 8. Closed-loop transfer functions under ideal grid with variable ω_c^{CC}: (a) PSC loop, (b) RPC loop.

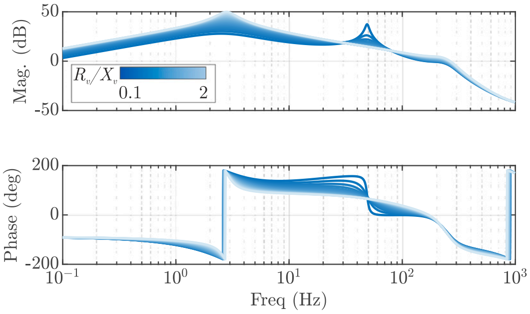

Fig. 9. Closed-loop Q/T dynamics with variable R_v/X_v.

SO mode, and excessive CC bandwidth causes HFO issues. An opposite effect of the virtual resistance-to-inductance on P/Q coupling and SO mode damping is revealed.

4.2. External stability

Assessing external stability involves analyzing interactions with a weak grid using the GNC method, which examines the Nyquist plot of the minor-loop gain $\boldsymbol{L}_{\mathbf{mlg}} = \boldsymbol{Z}_g \boldsymbol{Y}_{\mathbf{dfig}}$. This requires calculating the dual-loop GFM Type-3 generator input admittance. To this aim, the aggregated full-order model proves effective. The block diagram in Fig. 2 shows that a stator voltage perturbation has: (1) a direct effect on stator current via RSC control loops, (2) a direct effect on GSC current via PLL and current control loops, and (3) an indirect effect on the GSC current through rotor-side power perturbations in the DFIG. These interactions result in stator self-admittance $\boldsymbol{Y}_{ss}$, GSC self-admittance $\boldsymbol{Y}_{gg}$, and stator-to-GSC mutual admittance $\boldsymbol{Y}_{sg}$. More specifically, the stator self-admittance is defined by the relation between stator-side voltage and current perturbations:

$$\boldsymbol{Y}_{ss} = \frac{\hat{\boldsymbol{i}}_s}{\hat{\boldsymbol{v}}_s} \tag{33}$$

The GSC self-admittance is defined by the relation between stator-side voltage perturbations and GSC-side current perturbations only due to the dynamics of the GSC output filter, i.e., neglecting any power perturbation transmitted from the stator terminals to the DC link through the DFIG. As such it is defined as:

$$\boldsymbol{Y}_{gg} = \left.\frac{\hat{\boldsymbol{i}}_g}{\hat{\boldsymbol{v}}_s}\right|_{\substack{K_{\boldsymbol{PrVs}}=0\\ K_{\boldsymbol{PrIs}}=0}} \tag{34}$$

Ultimately, the stator-to-GSC mutual admittance represents the effect of stator voltage perturbations on the GSC currents only due to rotor-side power perturbations caused by the DFIG dynamics, i.e.:

$$\boldsymbol{Y}_{sg} = \left.\frac{\hat{\boldsymbol{i}}_g}{\hat{\boldsymbol{v}}_s}\right|_{\substack{K_{\boldsymbol{PcVs}}=0\\ G_{\boldsymbol{igvs}}=0\\ G_{\boldsymbol{ig\theta}}=0}} \tag{35}$$

Letting $\hat{P}^* = 0$ and $\hat{Q}^* = 0$ in the aggregated block diagram and rearranging, the following expressions are obtained for the three admittances:

$$\boldsymbol{Y}_{ss} = \boldsymbol{\Psi}^{-1}\left[G_{LPF}(R_{PSC}\boldsymbol{G}_{\boldsymbol{is\theta}}\boldsymbol{k}_{\boldsymbol{Tvs}} + R_Q\boldsymbol{G}_{\boldsymbol{isEk_{Qvs}}}) - \boldsymbol{G}_{\boldsymbol{isvs}}\right] \tag{36}$$

$$\boldsymbol{Y}_{sg} = \boldsymbol{Y}^{-1}\boldsymbol{G}_{\boldsymbol{igc}}\boldsymbol{R}_{\boldsymbol{V}}G_{dc}(\boldsymbol{k}_{\boldsymbol{PrVs}} - \boldsymbol{k}_{\boldsymbol{PrIs}}\boldsymbol{Y}_{ss}) \tag{37}$$

$$\boldsymbol{Y}_{gg} = \boldsymbol{Y}^{-1}(\boldsymbol{G}_{\boldsymbol{ig\theta}}\boldsymbol{k}_{\boldsymbol{PLL}} + \boldsymbol{G}_{\boldsymbol{igvs}} - \boldsymbol{G}_{\boldsymbol{igc}}\boldsymbol{R}_{\boldsymbol{V}}G_{dc}\boldsymbol{k}_{\boldsymbol{PcVs}}) \tag{38}$$

where

$$\boldsymbol{\Psi} = \mathbf{I} + G_{LPF}(R_{PSC}\boldsymbol{G}_{\boldsymbol{is\theta}}\boldsymbol{k}_{\boldsymbol{Tis}} + R_Q\boldsymbol{G}_{\boldsymbol{isE}}\boldsymbol{k}_{\boldsymbol{Qis}}), \quad \boldsymbol{Y} = \mathbf{I} + \boldsymbol{G}_{\boldsymbol{igc}}\boldsymbol{R}_{\boldsymbol{V}}G_{dc}\boldsymbol{k}_{\boldsymbol{PcIg}}$$

Since the stator-side and GSC-side of the generator are connected in parallel at the PCC, it follows:

$$\boldsymbol{Y}_{\mathbf{dfig}} = \boldsymbol{Y}_{ss} + \boldsymbol{Y}_{gg} + \boldsymbol{Y}_{sg} \tag{39}$$

Close inspection of (36) confirms that the transfer function $\boldsymbol{G}_{\boldsymbol{isvs}}$ is a high-frequency approximation for the total stator self-admittance. In fact, $\boldsymbol{Y}_{ss} = \boldsymbol{G}_{\boldsymbol{isvs}}$ if the low-bandwidth PSC and RPC loops are neglected, i.e., letting $R_{PSC} = R_Q = 0$. Therefore, the input-admittance provided here is an extension of the small-signal model provided in [27] to the low-frequency range.

Fig. 10(a)–(b) illustrate the Nyquist plot of $\boldsymbol{L}_{\mathbf{mlg}}$ as Z_v magnitude varies from 0.25 to 0.1 p.u. for a grid SCR of 5 and 2. The system remains internally stable, but unstable weak-grid interactions can be triggered. External stability is maintained up to $Z_v = 0.15$ p.u. for SCR of 5; beyond this, critical encirclements occur in the Nyquist plot. For SCR of 2, the stability margin increases to $Z_v = 0.2$ p.u., indicating a need for greater virtual impedance in weaker grids. Fig. 10(c) presents

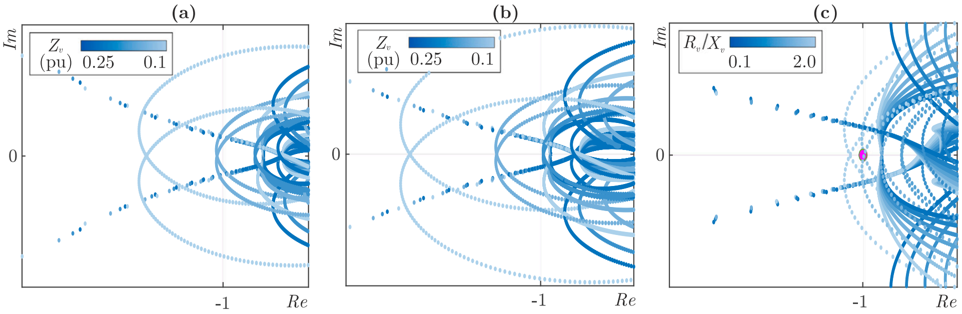

Fig. 10. GNC plots for variable Z_v: (a) $|Z_v|$ varies from 0.25 to 0.1 p.u. with $R_v/X_v = 0.5$ and SCR = 5 (b) $|Z_v|$ varies from 0.25 to 0.1 p.u. with $R_v/X_v = 0.5$, SCR = 2 (c) R_v/X_v varies from 0.1 to 2.0 p.u. with $|Z_v| = 0.5$ and SCR = 2.

the generalized Nyquist plot of the minor loop gain for an SCR of 2 with R_v/X_v varied from 0.1 to 2.0 p.u, which has been found to ensure internal stability. Unlike the strong-grid configuration, higher virtual resistance in a weak grid leads to instability at R_v/X_v above 1.75 p.u, with unstable HFO modes appearing at 265–275 Hz due to poor tuning. These unstable HFO interactions between the VA control parameters and weak grid impedance have not been revealed in [27].

4.3. Grid impact on closed-loop dynamics

Closed-loop transfer-function models including external grid parameters are used to evaluate how different grid conditions affect the dynamic response of PSC, RPC and DVC loops. Based on the derived full-order model and the stator and GSC self and mutual admittances (36)–(38), diagonal and mutual closed-loop reference-to-output and frequency disturbance-to-output transfer functions with weak grid are obtained. For the PSC, the following responses to reference variations, grid frequency disturbance and phase jump are obtained:

$$\hat{P}/\hat{P}^{*} = \left[\boldsymbol{k}_{\boldsymbol{Pis}} + (\boldsymbol{k}_{\boldsymbol{Pvs}} - \boldsymbol{k}_{\boldsymbol{Pis}}\boldsymbol{Y}_{\boldsymbol{ss}})\boldsymbol{Z}_{\boldsymbol{eq}}\right]\boldsymbol{F}_{\boldsymbol{isP}} \tag{40}$$

$$\hat{P}/\hat{\omega}_g = \left[\boldsymbol{k}_{\boldsymbol{Pis}} + (\boldsymbol{k}_{\boldsymbol{Pvs}} - \boldsymbol{k}_{\boldsymbol{Pis}}\boldsymbol{Y}_{\boldsymbol{ss}})\boldsymbol{Z}_{\boldsymbol{eq}}\right]\boldsymbol{F}_{\boldsymbol{is\omega}}/s \tag{41}$$

$$\hat{P}/\hat{\theta}_g = \left[\boldsymbol{k}_{\boldsymbol{Pis}} + (\boldsymbol{k}_{\boldsymbol{Pvs}} - \boldsymbol{k}_{\boldsymbol{Pis}}\boldsymbol{Y}_{\boldsymbol{ss}})\boldsymbol{Z}_{\boldsymbol{eq}}\right]\boldsymbol{F}_{\boldsymbol{is\omega}} \tag{42}$$

with

$$\begin{cases} \boldsymbol{F}_{\boldsymbol{isP}} = \boldsymbol{H}^{-1}\boldsymbol{G}_{\boldsymbol{is\theta}}R_{PSC}, \ \boldsymbol{F}_{\boldsymbol{is\omega}} = \boldsymbol{H}^{-1}\boldsymbol{G}_{\boldsymbol{is\theta}} \\ \boldsymbol{H} = \left[\mathbf{I} + G_{LPF}(R_{PSC}\boldsymbol{G}_{\boldsymbol{is\theta}}\boldsymbol{k}_{\boldsymbol{Pis}} + R_Q\boldsymbol{G}_{\boldsymbol{isE}}\boldsymbol{k}_{\boldsymbol{Qis}})\right], \end{cases}$$

and $\boldsymbol{Z}_{\boldsymbol{eq}} = (\boldsymbol{Y}_{\mathbf{dfig}} + \boldsymbol{Z}_{\boldsymbol{g}}^{-1})^{-1}$. The closed-loop PSC and reactive-to-active power responses with the SCR varying from 300 to 2 are shown in Fig. 11. The active power response to a grid frequency disturbance and to a grid voltage phase jump for the same SCR variation is shown in Figs. 12–13.

With a lower SCR, the PSC and power-to-frequency response bandwidth decreases while damping increases, reducing the transient inertial power provision availability and thus yielding a smaller virtual inertia effect from the GFM control. The power response is nearly overdamped for SCR < 3. Similar RPC loop dynamics occur. A frequency disturbance also excites an SO mode in the system, manifested by a local peak in the frequency response around 50 Hz. The damping of this SO mode is observed to decrease in stronger grids. This trend is attributed to the damping contribution of the grid resistance, whose influence diminishes as the SCR at the PCC increases. The SO mode due to frequency disturbance has lower damping in stronger grids. On the other hand, the steady-state frequency droop remains unaffected by SCR, while a stronger grid enhances the active-to-reactive power coupling, as the Q/P gain drops with lower SCR. The active power-to-phase jump response displays a dominant derivative effect at low frequencies and a SO mode that is similar to that described for the power-to-frequency coupling. The derivative response of the PSC to a phase jump tends to become less pronounced with a lower SCR.

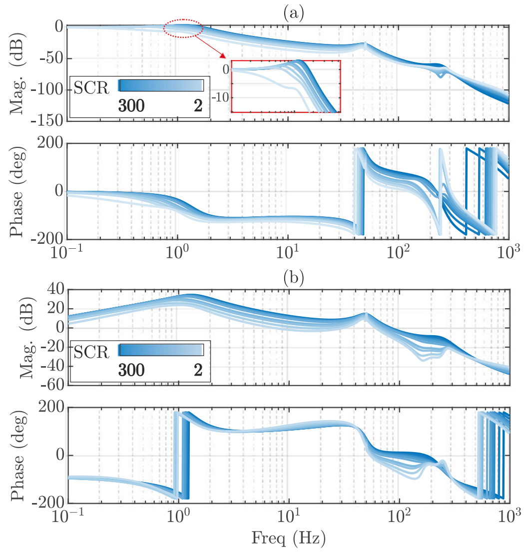

Fig. 11. Closed-loop dynamics for variable SCR: (a) PSC dynamics; (b) Q/P dynamics.

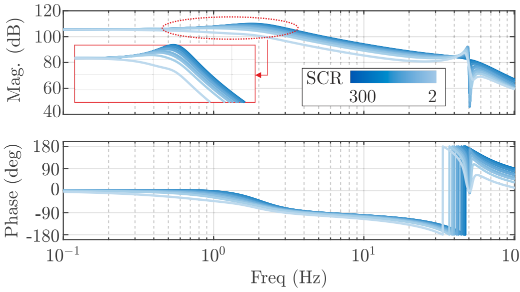

Fig. 12. Closed-loop P/ω_g dynamics for variable SCR.

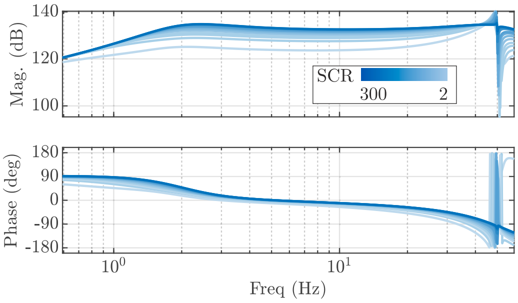

Fig. 13. Closed-loop P/θ_g dynamics for variable SCR.

Table 2
Comparison of existing studies.

		[6]	[7]	[26]	[27]	This work
Model	DFIG	Yes[a]	Yes	No	Yes	Yes
	DC link and GSC control	No	No	No	Yes	Yes
	RSC control	P/Q loops only	P/Q loops only[b]	P/Q loops only	v/i loops only	P/Q and v/i loops
	Control and PWM delays	No	No	No	No	Yes
Analysis	LFO issues	Yes	No	Yes	No	Yes
	SO issues	No	No	No	No	Yes
	HFO issues	No	No	No	No	Yes
	P/Q Coupling	No	No	No	No	Yes
	Frequency and phase perturbations	Yes[c]	No	Yes[c]	No	Yes

[a] Rotor only.
[b] With current limiting.
[c] Not modeled, EMT simulations only.

Likewise, the damping of the SO mode triggered by a phase jump increases with a lower SCR. While a similar influence of SCR on the torque response is reported in [6,26], its impact on the *P*–*Q* coupling and on the damping of SO modes under grid-frequency disturbances was not revealed.

An overall comparison of modeling accuracy and addressed stability issues between the present work and existing literature on GFM Type-3 wind generators is presented in Table 2.

5. Simulation results

To validate the design-oriented internal and external stability analysis presented in the previous section, a time-domain simulation of the GFM Type-3 wind generator is created in MATLAB/Simulink. The simulation model employs non-linear EMT Simscape® model blocks for the wind generator and power converters and provides a benchmark platform to validate the derived frequency-domain full-order model and design-oriented stability analysis. The simulation neglects switching harmonics, since the small-signal model is valid up to half the sampling frequency.

5.1. Frequency-domain validation

As an initial validation step, the closed-loop transfer functions and input admittance predicted by the derived model are compared with those obtained from frequency-scan simulations. To this end, a series of simulations is performed in which one input at a time is excited over a wide frequency range while the corresponding system outputs are recorded. At each frequency of interest, the numerical transfer function from input to output is then obtained as the ratio between the fast Fourier transforms (FFTs) of the output and the input signals.

First, the input-to-output torque and reactive power transfer functions are analyzed. The reference signals $\hat{P}^*$ and $\hat{Q}^*$ span a frequency range from 1 to 300 Hz. Fig. 14 presents the comparison with the predictions obtained from the full-order model based on the SISO equivalent block diagram of Fig. 4. As visible from the plot, the derived full-order model very well matches with data obtained from the full nonlinear simulation model and is able to capture all the dominant dynamics within a broad frequency spectrum.

A similar comparison is carried out for the input admittance of the GFM Type-3 generator. In the frequency-scan simulation, a voltage perturbation $\hat{\boldsymbol{v}}_s$ is superimposed on the stator voltages, and the PCC currents are recorded. The measured input admittance is then compared with the analytical expression given in (36)–(39). The results are presented in Fig. 15 and show an accurate match, which further validates the correctness of the presented full-order small-signal modeling procedure.

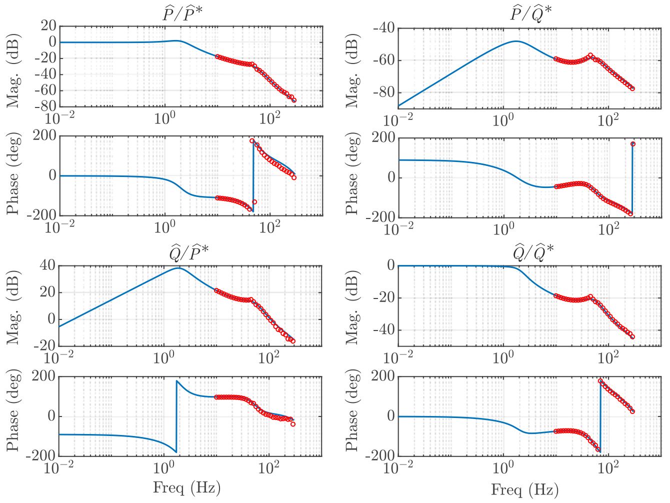

Fig. 14. Comparison between analytical model (blue solid line) and frequency-scan simulation data (red circles) of closed-loop PSC and RPC transfer functions.

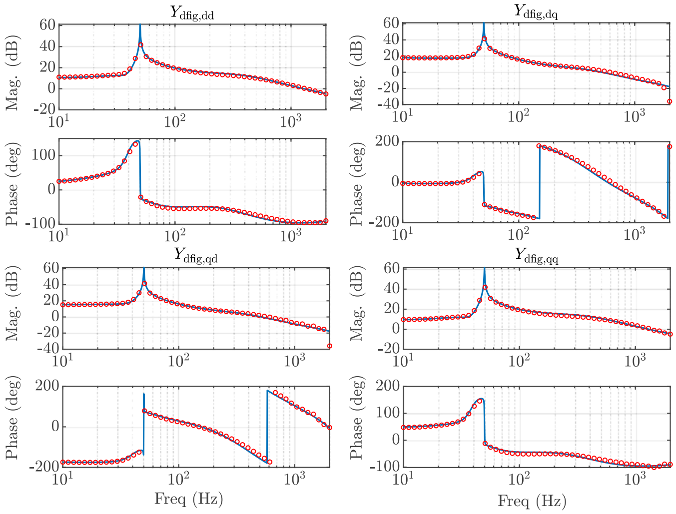

Fig. 15. Comparison between analytical model (blue solid line) and frequency-scan simulation data (red circles) of Type-3 generator closed-loop input admittance.

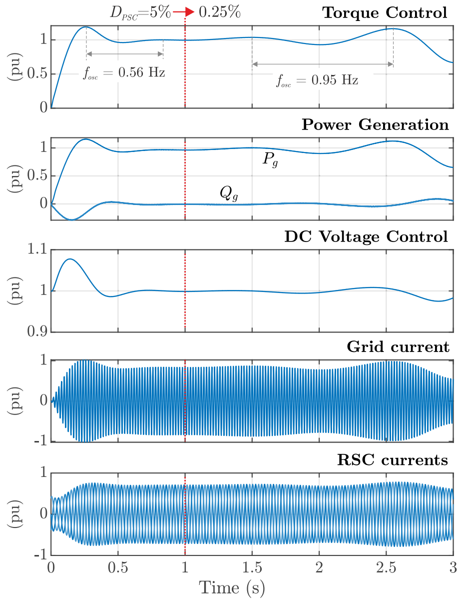

Fig. 16. Results for internal stability evaluation: variation in D_{PSC}.

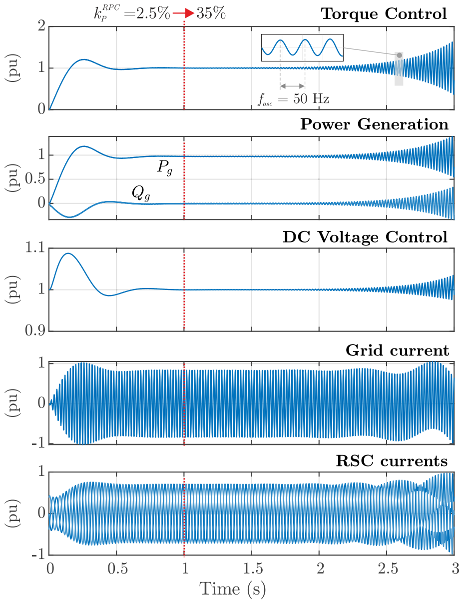

Fig. 17. Results for internal stability evaluation: variation in k_p^{RPC}.

5.2. *Internal stability margins*

As required by internal stability validation, the system is simulated under stiff grid connection. A step change in reference torque from 0 to 1 p.u. is commanded, with control parameters from Table 1. At $t = 1$ s, a control parameter is altered to verify the internal stability predictions obtained in Section 4.1.

Fig. 16 depicts the system response when the PSC droop gain decreases from 5% to 0.25%. The response shows an unstable LFO at about 0.95 Hz with negative damping, affecting torque, power, and voltage waveforms, and modulating both grid and RSC currents. This instability is accurately predicted by the analytical closed-loop PSC response in Fig. 5(a), which shows a pair of unstable poles when D_{PSC} drops below 0.3%.

Fig. 17 shows the system response when the RPC proportional gain is increased from 2.5% to 35%. As visible, the system is destabilized and exhibits oscillations near the synchronous frequency, with low-frequency amplitude modulation observed in RSC and PCC currents. This behavior is correctly matched by the RPC frequency response predicted by the model in Fig. 7(b), which clearly suggests unstable SO poles when k_p^{RPC} increases above 30%.

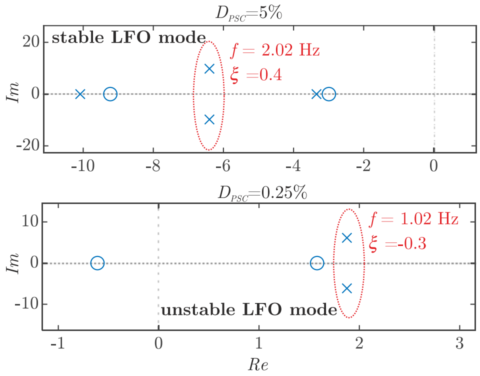

Fig. 18. Zero-pole map for D_{PSC} = 5% (stable LFO) and D_{PSC} = 0.25% (unstable LFO) obtained from the full-order small-signal model.

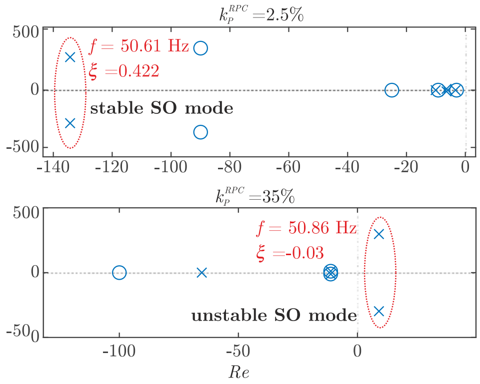

Fig. 19. Zero-pole map for k_p^{RPC} = 2.5% (stable SO) and k_p^{RPC} = 35% (unstable SO) obtained from the full-order small-signal model.

The pole movement shown in Figs. 18–19 yields further quantitative validation of the model predictions for the discussed LFO and SO instability mechanisms. The LF-mode poles move from the left to the right half-plane as the PSC droop gain reduces, predicting a 1.02 Hz oscillation with a damping ratio of −0.3. Similarly, SO-mode poles shift to unstable region and yield an unstable SO at 50.86 Hz with negative damping of −0.03 as the RPC proportional gain is set to 35%.

Fig. 20 illustrates how increasing the GSC and RSC control bandwidth from 200 Hz to 320 Hz causes unstable oscillations around 308 Hz in torque, power, and DC voltage. This unstable behavior matches with RHP poles predicted by the model in the PSC and RPC transfer functions above 300 Hz (see Fig. 8).

5.3. *Unstable interactions with the grid*

To validate the stability predictions obtained in Section 4.2 for a GFM Type-3 generator interacting with a weak grid, the system is simulated with a SCR of 2 at the PCC, as shown in Fig. 21. Starting from a stable control set, a unit torque step is commanded, and the VA magnitude is then reduced from 0.25 to 0.2 p.u. at 1.8 s. The instability mechanisms predicted by the model at 260 Hz well matches with the HFO observed in torque, power, and DC voltage responses at a frequency of 255 Hz. Increasing the virtual resistance-to-inductance ratio to 1.8 yields similar results, which are omitted for brevity. The close match between simulations and impedance modeling validates

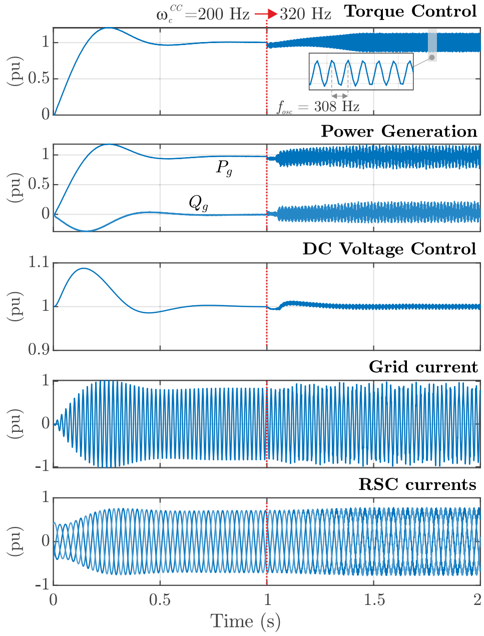

Fig. 20. Results of internal stability evaluation: variation in ω_c^{CC}.

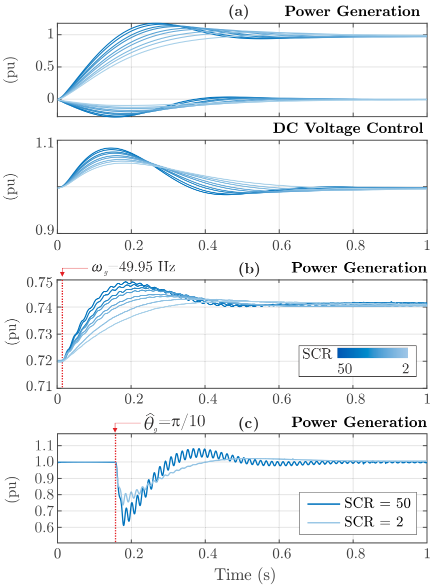

Fig. 22. Results for variable SCR: (a) step torque reference, (b) step grid frequency variation.

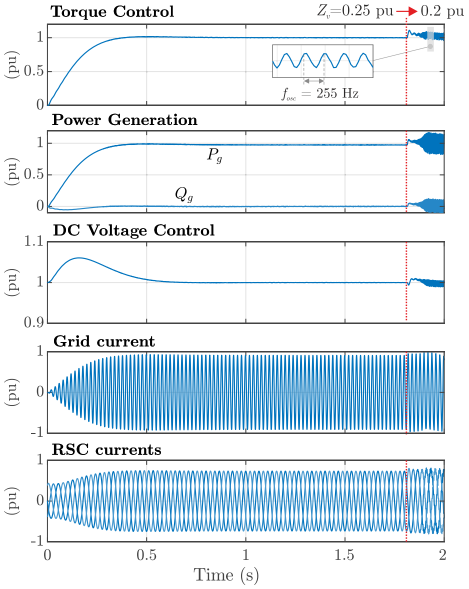

Fig. 21. Results for external stability evaluation: variable $|Z_v|$ with a SCR of 2.

the external stability predictions yield by the derived model and underscores the importance of proper VA tuning to maintain the stability of the Type-3 GFM generator under weak grid conditions.

5.4. Grid impact on closed-loop dynamics

A last simulation set is carried out to validate the analysis presented in Section 4.3 for closed-loop interactions between GFM Type-3 generator and grid under different SCR conditions. As the grid impedance rises, the PSC dynamics exhibit increased damping and slower response, resulting in an overdamped state for SCR below 3 as in Fig. 22(a). This affects the generator inertial response to frequency changes, as seen in Fig. 22(b) with a 0.1% frequency drop. The results show that a lower SCR yields and overdamped torque response, reducing the frequency-regulation effect of the virtual inertia which becomes lower, in agreement with the theoretical model predictions. The SO mode in the response to grid disturbances is also noticeable, and its damping increasing as the SCR decreases. The DVC is also impacted, with a smaller voltage deviation from the rated level when the SCR is low. The coupling between active and reactive power is stronger with low grid impedance. The PSC dynamic response to a phase jump in the grid voltages is shown in Fig. 22(c). Two main dynamics appear in the power-to-phase-jump response: a slow transient as the PSC restores the angle corresponding to the target power, and an SO mode associated with the virtual admittance control and grid dynamics. As in the frequency-disturbance case, the time-domain phase-jump response agrees well with the frequency-domain model: the PSC shows a weaker initial derivative effect, returns to the power setpoint with a slower and more damped transient, and excites an SO mode that is much more strongly damped at low SCR than at high SCR.

In conclusion, the time-domain EMT simulation results align with the transfer function-based modeling and design-oriented analysis of the system-grid interaction. The analysis suggests that PSC loop of the GFM Type-3 system should be tuned in the weaker grid case for adequate inertial power provision with given damping. Conversely, the resistance-to-inductance ratio in the VA should be configured in the stronger grid case to properly damp the SO mode excited by frequency and phase-jump perturbations.

6. Conclusion

This work has presented a comprehensive full-order modeling and design-oriented dynamic analysis of a Type-3 wind generator system employing dual-loop grid-forming control. The model accounts for discrete-time dynamics, stator-to-rotor and control loops couplings, converters, and frequency disturbances. It is compactly structured, allowing controller modifications without recalculating all subsystem transfer functions.

The modeling framework was used to analyze stability and dynamics under various control and grid conditions. It revealed control-grid interactions that affect oscillation modes in a wide frequency spectrum, especially in weak grids. In detail, some specific design-oriented prescriptions have been obtained for the dual-loop GFM Type-3 wind generator, which are as follows. The PSC dynamics can cause LFO instability, which can be mitigated by a higher torque droop and damping. The RPC impacts SO modes, improved by reducing RPC droop gain. The virtual impedance is vital for external stability in weak grids, requiring increased impedance for effective damping. However, a larger virtual inductance reduces the virtual inertial power provision and damping of the PSC loop.

In conclusion, the presented full-order modeling and design-oriented analysis allows to ensure internal and external stability margins as well as defined inertial and damping of the GFM Type-3 wind generator across different grid conditions.

CRediT authorship contribution statement

Emanuele Fedele: Writing – review & editing, Writing – original draft, Software, Investigation, Formal analysis, Conceptualization. **Nicola Campagna:** Writing – review & editing, Writing – original draft, Software, Investigation, Formal analysis. **Giuseppe Bossi:** Writing – review & editing, Writing – original draft, Validation, Software, Investigation, Formal analysis. **Renato Rizzo:** Writing – review & editing, Supervision, Project administration, Methodology. **Rosario Miceli:** Writing – review & editing, Supervision, Resources, Methodology. **Alfonso Damiano:** Writing – review & editing, Supervision, Resources, Project administration.

Declaration of competing interest

The authors declare that they have no known competing financial interests or personal relationships that could have appeared to influence the work reported in this paper.

Appendix

Steady-state linearization point:

$$\begin{cases} I_{sd0} = \dfrac{V_{g0}\sin\delta_g}{\omega_s L_g(1-\sigma_{sl}) + R_g\tan\varphi} \\ I_{sq0} = -\dfrac{V_{g0}\sin\delta_g\tan\varphi}{\omega_s L_g(1-\sigma_{sl}) + R_g\tan\varphi} \end{cases} \quad \begin{cases} I_{rd0} = \dfrac{L_s}{L_m} I_{sd0} \\ I_{rq0} = \dfrac{L_s}{L_m} I_{sq0} - \dfrac{V_{sd0}}{\omega_s L_m} \end{cases}$$

$$\times \begin{cases} I_{gd0} = -\sigma_{sl} I_{sd0} \\ I_{gq0} = 0 \end{cases}$$

$$\begin{cases} V_{rd0} = R_r I_{rd0} - \omega_{sl0}\left(L_r I_{rq0} - L_m I_{sq0}\right) \\ V_{rq0} = R_r I_{rq0} + \omega_{sl0}\left(L_r I_{rd0} - L_m I_{sd0}\right) \end{cases} \quad \begin{cases} V_{cd0} = V_{sd0} \\ V_{cq0} = V_{sq0} - \omega_s L_f I_{gd0} \end{cases}$$

Active and reactive power gains:

$$\boldsymbol{k_{PIs}} = \frac{3}{2} p\omega_{r0}\left(L_s\left[I_{sq0}, -I_{sd0}\right] + L_m\left[-I_{rq0}, I_{rd0}\right]\right), \;\; \boldsymbol{k_{QIs}} = \frac{3}{2}[V_{sq0}, -V_{sd0}]$$

$$\boldsymbol{k_{PVs}} = -\frac{3}{2} p\omega_{r0} L_s [I_{sq0}, -I_{sd0}]\boldsymbol{G_{Ls}^{-1}}, \;\; \boldsymbol{k_{QVs}} = \frac{3}{2}[-I_{rq0}, I_{rd0}]$$

Rotor-side power perturbation terms:

$$\boldsymbol{k_{PrIs}} = \frac{3}{2}\frac{2R_r L_s + s(L_r L_s - L_m^2)}{L_m}\begin{bmatrix} I_{rd0} & I_{rq0} \end{bmatrix} + \frac{3}{2}\frac{\omega_{sl0}}{\omega_s}\begin{bmatrix} V_{sd0} & V_{sq0} \end{bmatrix} \tag{A.1}$$

$$\boldsymbol{k_{PrVs}} = -\frac{3}{2}\frac{sL_r + 2R_r}{L_m}\begin{bmatrix} I_{rd0} & I_{rq0} \end{bmatrix} + \frac{3}{2}\omega_{sl0}\begin{bmatrix} -I_{sq0} & I_{sd0} \end{bmatrix}$$

Discrete-time virtual admittance implementation :

$$\boldsymbol{Y_v}(z) = \frac{\begin{bmatrix} n_{00} + n_{01}z^{-1} + n_{02}z^{-2} & n_{10} + n_{11}z^{-1} + n_{12}z^{-2} \\ -n_{10} - n_{11}z^{-1} - n_{12}z^{-2} & n_{00} + n_{01}z^{-1} + n_{02}z^{-2} \end{bmatrix}}{d_0 + d_1 z^{-1} + d_2 z^{-2}} \tag{A.2}$$

$$\begin{cases} n_{00} = R_v T_s^2 + 2L_v T_s, \quad n_{01} = 2R_v T_s^2, \quad n_{02} = R_v T_s^2 - 2L_v T_s \\ n_{10} = L_v T_s^2 w_s, \quad n_{11} = 2L_v T_s^2 w_s, \quad n_{12} = L_v T_s^2 w_s \\ d_0 = L_v^2 T_s^2 w_s^2 + 4L_v^2 + 4L_v R_v T_s + R_v^2 T_s^2 \\ d_1 = 2L_v^2 T_s^2 w_s^2 - 8L_v^2 + 2R_v^2 T_s^2 \\ d_2 = L_v^2 T_s^2 w_s^2 + 4L_v^2 - 4L_v R_v T_s + R_v^2 T_s^2 \end{cases}$$

Discrete-time PLL dynamics:

$$G_{PLL}(z) = \frac{\left(T_s k_p^{PLL}\right)z^{-1} + (T_s^2 k_i^{PLL} - T_s k_p^{PLL})z^{-2}}{1 + \left(T_s k_p^{PLL} - 2\right)z^{-1} + (T_s^2 k_i^{PLL} - T_s k_p^{PLL} + 1)z^{-2}}$$

Open-loop stator-side transfer functions:

$$\boldsymbol{G_{is\theta}} = \boldsymbol{\Lambda}^{-1}\left[\boldsymbol{\Sigma_1 k_{Vs\theta}} + \boldsymbol{\Sigma_2 T_\theta k_{Ir\theta}} + \boldsymbol{\Sigma_3 k_{Vs\theta}} + G_d \boldsymbol{k_{Vr\theta}}\right] \tag{A.3}$$

$$\boldsymbol{G_{isE}} = \boldsymbol{\Lambda}^{-1}\frac{L_s}{L_m} G_d \boldsymbol{T_\theta G_{cc}^{rsc} Y_v}\begin{bmatrix} 1 \\ 0 \end{bmatrix} \tag{A.4}$$

$$\boldsymbol{G_{isvs}} = \boldsymbol{\Lambda}^{-1}\left[\left(\boldsymbol{\Sigma_1} + \boldsymbol{\Sigma_3}\right)\boldsymbol{T_\theta^{-1}} + \boldsymbol{\Sigma_4 G_{Ls}^{-1}}\right] \tag{A.5}$$

with

$$\begin{cases} \boldsymbol{\Lambda} = \left[\dfrac{L_s}{L_m}\boldsymbol{G_{Lr}} - \dfrac{L_s}{L_m} G_d \boldsymbol{T_\theta}\left(\boldsymbol{K_{dcpl}^{rsc}} - \boldsymbol{G_{cc}^{rsc}}\right)\boldsymbol{T_\theta^{-1}}\right] \\ \boldsymbol{\Sigma_1} = G_d \boldsymbol{T_\theta G_{cc}^{rsc}}\left(\boldsymbol{K_{Vscmp}} - \dfrac{L_s}{L_m}\boldsymbol{Y_v}\right) \\ \boldsymbol{\Sigma_2} = G_d \boldsymbol{T_\theta}\left(\boldsymbol{K_{dcpl}^{rsc}} - \boldsymbol{G_{cc}^{rsc}}\right)\boldsymbol{T_\theta^{-1}} \\ \boldsymbol{\Sigma_3} = G_d \boldsymbol{T_\theta K_{Vrcmp}} \\ \boldsymbol{\Sigma_4} = \dfrac{L_s}{L_m}\boldsymbol{G_{Lr}} - \boldsymbol{G_{Lm}} - \dfrac{L_s}{L_m}\boldsymbol{\Sigma_2} \end{cases}$$

Open-loop grid-converter-side transfer functions:

$$\boldsymbol{G_{igc}} = -\boldsymbol{\Gamma}^{-1} G_d \boldsymbol{G_{cc}^{gsc}} \tag{A.6}$$

$$\boldsymbol{G_{ig\theta}} = -\boldsymbol{\Gamma}^{-1} G_d\left[\left(\boldsymbol{K_{dcpl}^{gsc}} - \boldsymbol{G_{cc}^{gsc}}\right)\boldsymbol{k_{Ig\theta}} + \boldsymbol{k_{Vs\theta}} + \boldsymbol{k_{Vc\theta}}\right] \tag{A.7}$$

$$\boldsymbol{G_{igvs}} = \boldsymbol{\Gamma}^{-1}\left(\mathbf{I} - G_d\mathbf{I}\right) \tag{A.8}$$

$$\boldsymbol{\Gamma} = G_d\left(\boldsymbol{K_{dcpl}^{gsc}} - \boldsymbol{G_{cc}^{gsc}}\right) + \boldsymbol{G_{Lf}} \tag{A.9}$$

Data availability

Data will be made available on request.

References

[1] Markovic U, Stanojev O, Aristidou P, Vrettos E, Callaway D, Hug G. Understanding small-signal stability of low-inertia systems. IEEE Trans Power Syst 2021;36:3997–4017.

[2] Rathnayake DB, Akrami M, Phurailatpam C, Me SP, Hadavi S, Jayasinghe G, Zabihi S, Bahrani B. Grid forming inverter modeling, control, and applications. IEEE Access 2021;9:114781–807.

[3] Yaramasu V, Wu B, Sen PC, Kouro S, Narimani M. High-power wind energy conversion systems: State-of-the-art and emerging technologies. Proc IEEE 2015;103:740–88.

[4] Okedu KE, Tobi MA, Araimi SA. Comparative study of the effects of machine parameters on DFIG and pmsg variable speed wind turbines during grid fault. Front Energy Res 2021;9.

[5] Oraa I, Samanes J, Lopez J, Gubia E. Modeling of a droop-controlled grid-connected DFIG wind turbine. IEEE Access 2022;10:6966–77.

[6] Wang S, Hu J, Yuan X. Virtual synchronous control for grid-connected DFIG-based wind turbines. IEEE J Emerg Sel Top Power Electron 2015;3:932–44.

[7] Nian H, Jiao Y. Improved virtual synchronous generator control of DFIG to ride-through symmetrical voltage fault. IEEE Trans Energy Convers 2020;35:672–83.

[8] Rodriguez-Amenedo JL, Gomez SA, Martinez JC, Alonso-Martinez J. Black-start capability of DFIG wind turbines through a grid-forming control based on the rotor flux orientation. IEEE Access 2021;9:142910–24.

[9] Rosso R, Wang X, Liserre M, Lu X, Engelken S. Grid-forming converters: Control approaches, grid-synchronization, and future trends—A review. IEEE Open J Ind Appl 2021;2:93–109.

[10] Leon JDV, Tarraso A, Candela JI, Rocabert J, Rodriguez P. Grid-forming controller based on virtual admittance for power converters working in weak grids. IEEE J Emerg Sel Top Ind Electron 2023;4:791–801.

[11] Huang L, Wu C, Zhou D, Blaabjerg F. Impact of virtual admittance on small-signal stability of grid-forming inverters. In: 2021 6th IEEE workshop on the electronic grid. EGRID, IEEE; 2021, p. 1–8.

[12] Huang L, Wu C, Zhou D, Chen L, Pagnani D, Blaabjerg F. Challenges and potential solutions of grid-forming converters applied to wind power generation system—An overview. Front Energy Res 2023;11. http://dx.doi.org/10.3389/fenrg.2023.1040781.

[13] D'Arco S, Suul JA, Fosso OB. A virtual synchronous machine implementation for distributed control of power converters in SmartGrids. Electr Power Syst Res 2015;122:180–97.

[14] Cao W, Ma Y, Wang F, Tolbert LM, Xue Y. Low-frequency stability analysis of inverter-based islanded multiple-bus AC microgrids based on terminal characteristics. IEEE Trans Smart Grid 2020;11:3662–76.

[15] Zhao L, Jin Z, Wang X. Small-signal synchronization stability of grid-forming converters with regulated DC-link dynamics. IEEE Trans Ind Electron 2023;70:12399–409.

[16] Guo J, Chen T, Chaudhuri B, Hui SYR. Stability of isolated microgrids with renewable generation and smart loads. IEEE Trans Sustain Energy 2020;11:2845–54.

[17] Amin M, Molinas M. Small-signal stability assessment of power electronics based power systems: A discussion of impedance- and eigenvalue-based methods. IEEE Trans Ind Appl 2017;53:5014–30.

[18] Yang D, Wang X. Unified modular state-space modeling of grid-connected voltage-source converters. IEEE Trans Power Electron 2020;35:9700–15.

[19] Cao W, Ma Y, Yang L, Wang F, Tolbert LM. D–Q impedance based stability analysis and parameter design of three-phase inverter-based AC power systems. IEEE Trans Ind Electron 2017;64:6017–28.

[20] Zhao F, Wang X, Zhou Z, Harnefors L, Svensson JR, Kocewiak LH, Gryning MPS. Control interaction modeling and analysis of grid-forming battery energy storage system for offshore wind power plant. IEEE Trans Power Syst 2022;37:497–507.

[21] Xu D, Blaabjerg F, Chen W, Zhu N. Advanced Control of Doubly Fed Induction Generator for Wind Power Systems. Wiley-IEEE Press; 2018.

[22] Xu Y, Nian H, Wang T, Chen L, Zheng T. Frequency coupling characteristic modeling and stability analysis of doubly fed induction generator. IEEE Trans Energy Convers 2018;33:1475–86.

[23] Hu J, Huang Y, Wang D, Yuan H, Yuan X. Modeling of grid-connected DFIG-based wind turbines for DC-link voltage stability analysis. IEEE Trans Sustain Energy 2015;6:1325–36.

[24] Zhang C, Cai X, Molinas M, Rygg A. Frequency-domain modelling and stability analysis of a DFIG-based wind energy conversion system under non-compensated AC grids: impedance modelling effects and consequences on stability. IET Power Electron 2019;12:907–14.

[25] Sun J, Vieto I. Development and application of Type-III turbine impedance models including DC bus dynamics. IEEE Open J Power Electron 2020;1:513–28. http://dx.doi.org/10.1109/OJPEL.2020.3040628.

[26] Wang S, Hu J, Yuan X, Sun L. On inertial dynamics of virtual-synchronous-controlled DFIG-based wind turbines. IEEE Trans Energy Convers 2015;30:1691–702, URL http://ieeexplore.ieee.org/document/7202890/.

[27] Huang L, Wu C, Zhou D, Blaabjerg F, Boldea I, He S. A decomposed two-port network impedance modeling method of Type-3 wind generation system with grid-forming control. In: 2023 IEEE energy conversion congress and exposition. ECCE, IEEE; 2023, p. 633–9.

[28] Zhang W, Cantarellas AM, Rocabert J, Luna A, Rodriguez P. Synchronous power controller with flexible droop characteristics for renewable power generation systems. IEEE Trans Sustain Energy 2016;7:1572–82.